Processes governing the predictability of the Atlantic Meridional Overturning Circulation in a coupled GCM

Pablo Ortega · Ed Hawkins · Rowan Sutton

Abstract The processes that govern the predictability of decadal variations in the North Atlantic Meridional Overturning Circulation (MOC) are investigated in a long control simulation of the ECHO-G coupled atmosphere-ocean model. We elucidate the roles of local stochastic forcing by the atmosphere, and other potential ocean processes, and use our results to build a predictive regression model. The primary influence on MOC variability is found to come from air-sea heat fluxes over the Eastern Labrador Sea. The maximum correlation between such anomalies and the variations in the MOC occurs at a lead time of 2 years, but we demonstrate that the MOC integrates the heat flux variations over a period of 10 years. The corresponding univariate regression model accounts for 74.5% of the interannual variability in the MOC (after the Ekman component has been removed). Dense anomalies to the south of the Greenland-Scotland ridge are also shown to precede the overturning variations by 4-6 years, and provide a second predictor. With the inclusion of this second predictor the resulting regression model explains 82.8% of the total variance of the MOC. This final bivariate model is also tested during large rapid decadal overturning events. The sign of the rapid change is always well represented by the bivariate model, but the magnitude is usually underestimated, suggesting that other processes are also important for these large rapid decadal changes in the MOC.

Keywords Decadal Predictability · Atmosphere Ocean General Circulation Model · Meridional Overturning Circulation

P. Ortega
Dpto. Astrofísica y Ciencias de la Atmósfera, Facultad de Ciencias Físicas, Universidad Complutense de Madrid, Ciudad Universitaria, 28040 Madrid, Spain
Tel.: +34-913945195
Fax: +34-913944635
E-mail: portegam@fis.ucm.es

E. Hawkins · R. Sutton
NCAS-Climate, Department of Meteorology, University of Reading, UK

1 Introduction

Development of successful climate predictions relies on a good representation of natural variability, especially in the ocean, as well as the climate response to external radiative forcings (Meehl et al, 2009). Recent advances in ocean initialization have led to improved decadal predictive skill globally, and for the North Atlantic region (Smith et al, 2007; Keenlyside et al, 2008; Pohlmann et al, 2009; Meehl et al, 2009). The skill of predictions for the North Atlantic relies particularly on a proper assimilation of persistent anomalies, like the ocean heat content (Smith et al, 2007; Meehl et al, 2009), and an accurate description of the mechanisms of internal variability, such as the subpolar gyre dynamics, and the meridional overturning circulation (MOC) (Keenlyside et al, 2008). The MOC is thought to account for a large fraction of the low-frequency (multi-decadal) variability in the Atlantic (Delworth and Mann, 2000; Knight et al, 2005), and it has been suggested to drive multi-decadal climate variability over North America and Europe (e.g. Sutton and Hodson, 2005; Collins et al, 2006). There is also evidence that the MOC may weaken in response to the predicted anthropogenic increase in high-latitude temperature and precipitation, although models show a wide spread in projections (Gregory et al, 2005; Meehl et al, 2007). There is also the possibility of a more rapid decrease, either as a response to anthropogenic forcings or because of a natural fluctuation, which would have major impacts on regional and global climate (e.g. Hall and Stouffer, 2001; Hawkins and Sutton, 2008).

The importance of the North Atlantic MOC for climate highlights the need for research to better understand the processes that govern its variability and predictability. Previous research has established that the MOC responds to variations in the formation of dense waters in the subpolar North Atlantic (e.g. Delworth et al, 1993; Timmermann et al, 1998). Deep water formation itself is subject to both local and non-local influences. Local influences are associated particularly with variations in the air-sea fluxes that modulate deep convection. Non-local influences may arise through advection or wave propagation in the ocean. Lateral mixing processes may give rise to interactions between local and non-local influences. The predictability of MOC variations depends, in substantial part, on the relative importance of these different influences, and on the detailed nature of each influence. The first aim of this study is to elucidate the roles of local stochastic forcing and other potential processes in governing MOC variability and predictability, in a particular coupled climate model.

The variability of air-sea fluxes on interannual and longer timescales is often assumed to be stochastic (Griffies and Tziperman, 1995; Saravanan and McWilliams, 1997; Kravtsov and Ghil, 2004; Monahan et al, 2008) and hence unpredictable. However, the influence on deep water formation of the variability in air-sea fluxes is not instantaneous (e.g. Delworth and Greatbatch, 2000; Eden and Willebrand, 2001). The ocean has significant memory, and consequently integrates the fluctuations over a period of time (e.g. Hasselmann, 1976; Frankignoul and Hasselmann, 1977). Less clear, for a particular application, is over *what* time period this integration occurs. In the case of deep water formation in the North Atlantic, the effective time period is an important matter, because it may determine the predictability of MOC fluctuations. Consequently, a second aim of this study is to investigate the extent to which the MOC integrates in time the influence of air-sea fluxes, and the consequences for MOC predictability.

The paper is based on analysis of a 1000 year control simulation of a coupled climate model, ECHO-G. The processes that govern decadal variability in the Atlantic MOC

in this model are elucidated and, based on the results, a predictive regression model is developed and tested. A complementary work (Ortega et al. 2010, submitted to Climate Dynamics) analyses other aspects of the MOC variability separately at interannual and interdecadal timescales in three long simulations with the ECHO-G model. This paper is structured as follows: in section 2 the model used is described, and the main features of the simulation are shown. The two major contributions to the overturning variability are analysed in sections 3 and 4, leading, respectively, to the calculation of a univariate and a bivariate regression model of the MOC. These models are tested in section 5 by analysing their skill in the prediction of rapid decadal overturning variations. Finally, the main results and conclusions are summarised in section 6.

2 Model and data description

The analysis has been performed with the ECHO-G (Legutke and Voss, 1999) coupled climate model, which consists of the atmosphere component ECHAM4 (Roeckner et al, 1996), and its ocean counterpart HOPE-G (Wolff et al, 1997). The atmosphere has a T30 horizontal resolution (approx. $3.75°$) and 19 vertical levels. The horizontal resolution of the ocean is about $2.8°$ x $2.8°$, with a grid refinement in the tropical regions, and 20 levels in the vertical. A comprehensive description about the model is given in González-Rouco et al (2009) and references therein. Here we use a 1000 year control run (CTRL), with fixed present day climate forcings. This model incorporates both heat and freshwater flux adjustments to avoid climate drift. Other aspects of the simulation have been explored by several authors (Zorita and González-Rouco, 2002; Zorita et al, 2003; von Storch et al, 2004; González-Rouco et al, 2003b, 2006, 2009; Beltrami et al, 2006). The first two centuries of CTRL are removed from the analysis to minimise the effects of ocean spin-up. Since this study focuses on interannual to interdecadal timescales, the remaining drift and long-term variability are also removed by detrending with a 3rd order polynomial. We focus our analysis on annual mean quantities.

2.1 Climatology and temporal variability

We now consider the relevant aspects of the MOC, as represented by this GCM. Figure 1a shows the mean MOC, which has a typical spatial structure, but the maximum overturning strength is found further north than in some other GCMs (e.g. Timmermann et al, 1998; Jungclaus et al, 2005; Dong and Sutton, 2005). A meridional overturning index (MOI) is defined locally at $47.4°$ N and 1050 m to represent the MOC temporal variability near its climatological maximum. The long-term mean of the MOI is 16.5 Sv, with a standard deviation of 1.8 Sv. For the following analysis the MOI has been detrended and normalised. Figure 1b shows that MOI oscillations tend to occur at decadal to interdecadal timescales, suggesting potential predictability. Indeed, the corresponding power spectrum (shown in the complementary paper Ortega et al. 2010) gives evidence of MOI variability other than pure red noise at interannual (periods from 2 to 5 years), and decadal timescales. In Figure 2 a Hovmoller diagram (latitude vs time) shows the variability of the integrated ocean transport down to 1050m, and highlights the different temporal scales of variability at different latitudes. It is clear that at higher latitudes the variability is predominantly decadal, whereas the tropics

are more noisy and therefore interannual is more prominent (similar to the HadCM3 GCM; Bingham et al, 2007). A slight tilt of the anomalies is visible in the latitude belt around 40-45°, indicating a localised slow-down in the southward propagation.

Figure 3 shows the main spatial features of North Atlantic convection in March (when events of deepest convection occur). The variability of convection is commonly represented by the variations of the Mixed Layer Depth (MLD). Unfortunately, this variable was not stored in the CTRL run, and we use the Potential Energy Released by Convection (PERC) instead (similarly to Timmermann et al, 1998). The variability of the PERC and the MLD has been compared in other simulations with the ECHO-G model, and they produce virtually identical results for both variables (not shown). The mean PERC pattern (Figure 3a) shows three main convection regions with comparable climatological values: the East Labrador, Central Irminger, and Norwegian Seas. More interestingly, variability of convection is considerably larger near the Labrador Sea (Figure 3b). ECHO-G is not eddy-resolving, and therefore the representation of deep water formation lacks some essential dynamics, that could explain the main discrepancies with respect to observations (Marshall and Schott, 1999), such as the rather eastern location of Labrador convection, or the relative small variance in the Norwegian Seas. Likewise, convection in Central Irminger Sea has been reported in other models (e.g. Guemas and Salas-Mélia, 2008; Lohmann et al, 2009; Msadek and Frankignoul, 2009), but is not supported by observations.

3 Influence of Labrador convection on the overturning.

Deep convection variations in the North Atlantic are thought to play an important role in determining MOC low-frequency variability. The occurrence of these convection events is influenced by local stochastic forcing from the atmosphere. This section is concerned with understanding how the ocean integrates the anomalous heat fluxes at the main region of deep water formation, and quantifying how the integrated signal contributes to the variance of the overturning.

3.1 The role of convection

The regression patterns between the Meridional Overturning Index (MOI) and the surface heat flux (HFL) anomalies in the convection regions are shown in Figure 4. Similar patterns emerge for the PERC (not shown), providing evidence of the role of the HFL on convection. Indeed, the largest HFL anomalies are found to the south of Greenland, in the same region as the maximum standard deviations of the PERC (Figure 3b). A significant influence of local heat fluxes on the MOC variability is observed during the 10 years preceding the large overturning anomalies (Figure 5). Moreover, the regression patterns of the HFL have similar spatial features for all lead times up to 10 years, and show their maximum regression coefficients when the HFL leads the overturning by 2 years (Figure 4; left panel). No clear influence of fresh water fluxes is observed on convection (not shown). Indeed, evaporation is inhibited as a response to the cooling of surface temperature forced by positive heat fluxes. Large overturning changes seem, therefore, to be triggered by persistent strong heat flux interaction with the atmosphere, favoured by an intensification of northwesterly winds over the Labrador Sea (vectors in Figure 4, blue line in Figure 5). A similar pattern of

heat flux and wind variations leading the overturning by 3 years was found by Delworth and Greatbatch (2000) in a previous version of the GFDL model, which they related to the North Atlantic Oscillation. In this case, however, the surface forcing is driven locally by negative SLP anomalies centred to the South of Greenland (black contours in Figure 4). At lag zero (Figure 4, right panel) the HFL pattern over the Labrador Sea is weakened, along with the local wind forcing. Simultaneously to the east, a pattern of anomalous easterlies emerges at midlatitudes, centred around $50°$N, where the MOI is defined.

3.2 Constructing the regression model

The local atmospheric influence on convection and thereby on the overturning is represented by the average of the heat flux anomalies to the South of Greenland (black rectangle in Figure 4). This timeseries is used to produce a univariate regression model for the overturning circulation,

$$MOI(t) = \alpha \sum_{i=1}^{L} \omega_i H(t-i) + \xi \tag{1}$$

where MOI represents the overturning index to reconstruct, α is the regression coefficient, ω is the weighting function for time integration, H is the predictor (i.e. the heat flux index), ξ accounts for the residuals, i is the lag in years and L is the maximum lag. To ensure that we are only using information prior to the variability being predicted, we use $i > 0$ only.

The main features of the heat flux integration are determined by considering different integration approaches. Since the magnitude of the HFL influence varies with time, three weighting schemes were tested. One is based on the correlation values in Figure 5, and the others make use of triangular and Gaussian weighting functions with different slopes and decay rates, respectively. Different time integration periods were also considered. The best univariate model is achieved using a Gaussian weighting function maximum at lag -2 (when the influence of convection is maximum; see Figure 5) that decays smoothly up to lag -10. It coincides with the period with non-negligible correlations between the MOC and the HFL index (Figure 5). This analysis therefore reveals that there is a decadal integration of the heat flux anomalies by the ocean. Using this approach the variance explained by the regression model is 69.6%, almost 20% higher than when no time integration is employed (Table 1).

The zero-lag correlation pattern between the residuals from the regression model and the wind stress anomalies (not shown) exhibits a band of mid-latitude anomalous easterlies near the latitude where the MOI is defined, similar to the eastern signal in Figure 4b. This is the part of the Ekman contribution which is unrelated to the first predictor, and will be removed for the construction of the regression model. The signal is isolated by calculating a simple linear regression between the average of the zonal wind stress at $43°$ N (latitude with the largest correlations) and the residuals from the univariate model. The resulting series is then filtered out of the raw MOI (dashed line in Figure 1b), and the univariate model is recalculated for the new index. As a result, the fraction of variance explained by the predictor increases, reaching a maximum value of 74.5% when the same time integration scheme is considered. In the remainder of the text MOI will refer to the Ekman-filtered overturning index.

3.3 Validating the univariate model

In order to validate the use of the HFL index as a predictor of the MOI variability, the simulation is divided into two halves and the univariate regression model is recalculated using the first half. The regression coefficients obtained for the initial period are now employed to reconstruct the MOI timeseries for the second part of the simulation. The reconstructed overturning (dashed line in Figure 6) is in good agreement with the real (Ekman-filtered) MOI, with a correlation value of 0.85. This same value is obtained if the reconstruction is performed using the regression coefficients from the whole timeseries. Therefore, the regression model is reasonably consistent throughout the whole run. However, the prediction tends to underestimate the variability at shorter timescales, as well as the magnitude of change during the largest overturning variations. A scatterplot analysis of the residuals over the second half of the simulation (solid points in Figure 7) reveals that the magnitude of the error is proportional to both the MOI (blue points; correlation coefficient, r = -0.49) and the decadal change preceding that event (yellow points; r = -0.38). If the regression model was consistent, both correlation values should be close to zero. In order to improve the regression model, the contribution of other different processes needs to be explored through an analysis of the residuals.

4 The bivariate regression model

The aim of this section is to analyse the influence of other processes in order to improve the regression model by defining a new predictor that extracts the maximum possible coherent variability from the residuals, whilst ensuring it has a physical basis to avoid overfitting. The relationship between the residuals and the main atmospheric and oceanic variables is explored by means of a time-lag correlation analysis. The largest signal is found for density anomalies in the Irminger Sea (Figure 8). Positive correlations are found in the upper ocean (0 to 800m) to the South of the Greenland-Scotland Ridge, about 4-6 years before the maximum of the overturning. This pool of dense waters appears to propagate westward, where it modifies the background stratification, and then propagates southward towards the Equator. At deeper levels (1000 to 1500m), a zonal density gradient is established between a pool of dense waters near the Irminger Sea (just South of the Denmark Strait) and a region of lighter waters in the vicinity of the British Isles. The zonal dipole persists as the positive density anomalies propagate along the western boundary. This propagation is reminiscent of the oscillation mechanism described by both Colin de Verdière and Huck (1999) and Te Raa and Dijkstra (2002), in which westward propagation of buoyancy anomalies produces zonal and meridional overturning responses.

A new predictor is defined by averaging the density anomalies in the upper 1500m of the western Irminger Sea (grey box in Figure 8). This new Irminger Sea density index (ISD) is related to an increase of convection from the Irminger Sea to the British Isles (Figure 9a), the same region occupied by the upper density anomalies in Figure 8. A similar band of dense waters, also related to convection, was identified by Msadek and Frankignoul (2009) in the IPSL model. They found that deep convection is activated by the advection of salty waters, responding to variations in the East Atlantic Pattern. The resulting changes in density led the overturning variations by about 3-5 years. A similar lead time is observed in our model (Figure 10). However, the origin of these

anomalies is rather different. Simultaneously to the increase of convection, there is an enhancement of the southward flow through the Denmark Strait (Figure 9b), and a local cyclonic gyre is formed to the East of Cape Farewell. As a result, cold waters from the Nordic Seas are advected to the East (Figure 9c), reaching the regions of convection, where they help to keep the water column destabilised. No influence of salinity anomalies is found in this case (Figure 9d).

The two predictors are now used to build a new bivariate regression model, described by the generic equation,

$$MOI(t) = \alpha \sum_{i=1}^{L} \omega_i H(t-i) + \beta \sum_{j=1}^{M} \sigma_j I(t-j) + \xi \qquad (2)$$

where, similarly to Equation 1, MOI corresponds to the Ekman-filtered overturning timeseries, α and β are the regression coefficients, ω and σ are the weights used for time integration, H and I are the two predictors (i.e. HFL and ISD respectively), and finally ξ is the term accounting for the residuals of the bivariate model.

The same weighting schemes and integration periods as considered for the HFL index are tested again for the ISD index. In this case, the best regression model is again obtained for a Gaussian function, but centred at lag -4 (when the correlations between the residuals from the univariate model and the ISD index are maximum; Figure 10). This Gaussian function decays rather fast as compared to that of the first predictor, thus suggesting a short-time influence of the ISD. As a consequence, the signal of this second predictor is integrated over a shorter period (i.e. 7 years) than for the HFL index. The variance explained by this bivariate model rises to 82.8%, i.e. an increase of more than an 8% with respect to the former univariate model.

A significant improvement is also found in the validation process. The bivariate regression model is again recalculated in the initial half of CTRL, and its regression coefficients are employed to reconstruct the overturning during the second half. The new reconstructed MOI (blue dotted line in Figure 6) is slightly better correlated with the true MOI (r = 0.87, instead of 0.85). The magnitude of change of the large overturning variations is generally better represented, although in some cases is clearly overestimated (Figure 6), for example at year 670. Perhaps more importantly, the bivariate model is more consistent, since the correlations between the residuals and both the MOI and the decadal change preceding them are clearly smaller (unfilled circles in Figure 7). A subsequent analysis of these bivariate residuals shows no clear evidence of another coherent oceanic or atmospheric influence.

5 Rapid decadal overturning events in the model

As a final step, the bivariate model is evaluated during large, rapid decadal changes in the MOI. These events are especially important, as they are likely to produce the largest climate impacts.

The largest decadal changes (both increases and decreases) in the MOI are identified, and their magnitudes are compared in Figure 11. There appears to be an asymmetry in the sign of the rapid changes, with positive rapid events generally being larger than the negative events. However, the two largest decadal changes are found to be rapid decreases in the MOI. The reasons for this possible asymmetry are not clear, and merit some further analysis that goes beyond the goals of this paper. We speculate

that it could be a consequence of the non-linear behaviour of convection.

Figure 12 collects all 13 of the episodes in which the decadal change is larger in magnitude than 3 standard deviations (i.e. ~ 5 Sv or $\sim 30\%$ of the mean MOI, 16.5 Sv). The evolution of both the true (Ekman-filtered), and the reconstructed MOI are shown, along with the leading signal of the two predictors. Since negative HFL variations are associated with increasing overturning events, the sign of this precursor has been reversed for the plot to ease interpretation. Although we cannot expect a precise correspondence between the actual and the predicted MOI timeseries, it is immediately clear that the sign of the change is well reproduced, but the magnitude is generally underestimated. In every event, the sign associated to the HFL is the one expected to explain the MOI variations. In contrast, the role of dense waters in the Irminger Sea is not always important, and its value is found to vary both in magnitude and sign. To conclude, the limitations of the regression model show that the largest decadal rapid events are subject to additional influences beyond the predictors identified herein.

6 Conclusions and discussion

The processes influencing the predictability of decadal variability in the North Atlantic MOC have been analysed in a long control simulation with the ECHO-G coupled climate model. The main findings can be summarized as follows:

- The MOC variability is influenced both by local variations in the Labrador and Irminger Seas; correspondingly, two predictors for MOC variability have been identified. By constructing a bivariate regression model it has been shown that these predictors can together account for 82.8% of the total interannual variance of the MOC, after the Ekman component has been removed.
- The first predictor is the anomalous heat flux averaged over a region in the Eastern Labrador Sea. It explains 74.5% of the variance in the MOC. Stochastic forcing from the atmosphere is integrated locally by the ocean and drives deep convection, and therefore the overturning. The atmospheric influence is largest at a lead time of 2 years, but the effective integration by the MOC extends to lead times up to 10 years.
- The second predictor is anomalous ocean density in a region of the Western Irminger Sea. In the upper ocean, dense waters begin to accumulate 6 years before the MOC is maximum. These waters are associated with a zonal density gradient at deeper levels, that leads to an enhancement of the western boundary current, and hence the overturning.
- The final regression model is obtained integrating the first predictor over 10 years, and the second over 7 years, both using gaussian integration schemes. Note that these results are specific to this model.
- The large, rapid changes (both decadal increases and decreases larger than 3 standard deviations) in the MOC are mainly related to the variations in the Eastern Labrador Sea, although other processes may play a role for these events. A possible asymmetry in the sign of large rapid decadal events is noted, with rapid increases being more common than rapid decreases.

The origin of the dense anomalies in the Irminger Sea is related to the variability of the outflows from the Nordic Seas. Hawkins and Sutton (2008) found that discharges of dense waters through the Denmark Strait preceded the rapid MOC changes in a long

Table 1 Variance explained by the regression models

	Raw HFL	Integ. HFL	Integ. HFL + Integ. ISD
Raw MOI	51.0%	69.6%	
No-Ekman MOI	54.8%	74.5%	82.8%

control simulation with the HadCM3 model. Besides, salinity variations in the Atlantic Inflow are known to influence the dynamics of the subpolar gyre (Hátún et al, 2005), which could in turn modify the large-scale density pattern. Our analysis supports the role of the outflow through the Denmark Strait, and an intensification of the gyre near the Irminger Sea to explain the cold dense waters South of the sill. It also suggests a further role of local convection in which anomalous surface heat fluxes over the Irminger Sea lead to the formation of density anomalies.

The major importance of local atmospheric forcing over non-local large-scale mechanisms is likely overestimated in the ECHO-G model. The contribution to MOC variability from advective processes is hampered by the coarse resolution. For example, the realism of the overflows is constrained by the inaccurate representation of ocean topography (e.g. Roberts and Wood, 1997). Furthermore, non-resolved dynamics lead to an unrealistic representation of the deep water formation regions, as well as to an underestimation of the strength of the subpolar gyre (15 Sv, not shown), well below the range of observational estimates (25 to 40 Sv; Clarke, 1984; Reynaud et al, 1995; Bacon, 1997).

Identification of predictors for MOC variability is important for ocean monitoring strategies. This study supports the key role of the subpolar North Atlantic, and in particular of the Labrador and Irminger Seas as found by many previous studies. However, in view of the model biases already described, inferences about the particular regions, the specific mechanisms and their corresponding timescales would require further evidence. Differences to expect in other studies are a change in the regions of convection, that could also modify the timescales of the heat flux integration, and also larger influence of advective and/or wave propagation processes. Despite the uncertainties, our results are physically consistent, and contribute to improve our understanding on the potential processes determining deep water formation.

Finally, the current study has been performed in a present day control integration with constant radiative forcings. It is not known whether the presence of external forcing variations (e.g. solar activity, volcanic and anthropogenic aerosols, greenhouse gas concentrations) would modify the modes of variability in the ocean, and therefore the validity of our MOC predictors. In further work the analysis will be extended to some forced simulations of the last millennium and some scenario simulations.

References

Bacon S (1997) Circulation and fluxes in the North Atlantic between Greenland and Ireland. J Phys Oceanogr 27:1420–1435

Beltrami H, González-Rouco JF, Stevens MB (2006) Subsurface temperatures during the last millennium: Model and observation. Geophys Res Lett 33:L09,705, DOI 10.1029/2006GL026050

Bingham R, Hughes C, Roussenov V, Williams R (2007) Meridional coherence of the North Atlantic meridional overturning circulation. Geophys Res Lett 34:L23,606, DOI 10.1029/2007GL031731

Clarke RA (1984) Transport through the cape farewell-flemish cap section. Rapp P V Reun Cons Int Explor Mer 185:120–130

Collins M, Botzet M, Carril A, Drange H, Jouzeau A, Latif M, Masina S, Ottera OH, Pohlmann H, Sorteberg A, Sutton RT, Terray L (2006) Interannual to Decadal Climate Predictability in the North Atlantic: A Multimodel-Ensemble Study. J Clim 19:1195–1203

Delworth TL, Greatbatch RJ (2000) Multidecadal Thermohaline Circulation Variability driven by atmospheric surface flux forcing. J Clim 13:1481–1495

Delworth TL, Mann ME (2000) Observed and simulated multidecadal variability in the Northern Hemisphere. Clim Dyn 16:661–676

Delworth TL, Manabe S, Stouffer RJ (1993) Interdecadal Variations in the Thermohaline Circulation in a Coupled Ocean-Atmosphere Model. J Clim 6:1993–2011

Dong B, Sutton RT (2005) Mechanism of Interdecadal Thermohaline Circulation Variability in a Coupled Ocean-Atmosphere GCM. J Clim 18:1117–1135

Eden C, Willebrand J (2001) Mechanism of Interannual to Decadal Variability of the North Atlantic Circulation. J Clim 14:2266–2280

Frankignoul C, Hasselmann K (1977) Stochastic climate models. Part II: Application to sea-surface temperature anomalies and thermocline variability. Tellus 29:289–305

González-Rouco FJ, Beltrami H, Zorita E, von Storch H (2006) Simulation and inversion of borehole temperature profiles in surrogate climates: Spatial distribution and surface coupling. Geophys Res Lett 33:L01,703, DOI 10.1029/2005GL024693

González-Rouco FJ, Beltrami H, Zorita E, Stevens MB (2009) Borehole climatology: a discussion based on contributions from climate modeling. Clim Past 5

González-Rouco JF, Zorita E, Cubasch U, von Storch H, Fisher-Bruns I, Valero F, Montavez JP, Schlese U, Legutke S (2003b) Simulating the climate since 1000 AD with the AOGCM ECHO-G. ESA SP 535:329–338

Gregory JM, Dixon KW, Stouffer RJ, Weaver AJ, Driesschaert E, Eby M, Fichefet T, Hasumi H, Hu A, Jungclaus JH, Kamenkovich IV, Levermann A, Montoya M, Murakami S, Nawrath S, Oka A, Sokolov AP, Thorpe RB (2005) A model intercomparison of changes in the Atlantic thermohaline circulation in response to increasing atmospheric CO_2 concentration. Geophys Res Lett 32:L12,703, DOI 10.1029/2005GL023209

Griffies SM, Tziperman E (1995) A Linear Thermohaline Oscillator Driven by Stochastic Atmospheric Forcing. J Clim 8:2440–2453

Guemas V, Salas-Mélia D (2008) Simulation of the atlantic meridional overturning circulation in an atmosphere–ocean global coupled model. part i: a mechanism governing the variability of ocean convection in a preindustrial experiment. Climate Dynamics 31:29–48, DOI 10.1007/s00382-007-0336-8

Hall A, Stouffer R (2001) An abrupt climate event in a coupled ocean–atmosphere simulation without external forcing. Nature 409:171–174

Hasselmann K (1976) Stochastic climate models. Part I: Theory. Tellus 28:473–484

Hátún H, Sandø A, Drange H, Hansen B, Valdimarsson H (2005) Influence of the Atlantic Subpolar Gyre on the Thermohaline Circulation. Science 309:1841–1844, DOI 10.1126/science.1114777

Hawkins E, Sutton R (2008) Potential predictability of rapid changes in the Atlantic meridional overturning circulation. Geophys Res Lett 35:L11,603, DOI 10.1029/2008GL034059

Jungclaus JH, Haak H, Latif M, Mikolajewicz U (2005) Arctic-North Atlantic Interactions and Multidecadal Variability of the Meridional Overturning Circulation. J Clim 18:4013–4031

Keenlyside N, Latif M, Jungclaus J, Kornblueh L, Roeckner E (2008) Advancing decadal-scale climate prediction in the North Atlantic sector. Nature 453:84–88, DOI 10.1038/nature06921

Knight JR, Allan RJ, Folland CK, Vellinga M, Mann ME (2005) A signature of persistent natural thermohaline circulation cycles in observed climate. Geophys Res Lett 32:L20,708, DOI 10.1029/2005GL024233

Kravtsov S, Ghil M (2004) Interdecadal Variability in a Hybrid Coupled Ocean–Atmosphere–Sea Ice Model. J Phys Oceanography 34:1756–1775

Legutke S, Voss R (1999) The Hamburg Atmosphere-Ocean Coupled Circulation Model ECHO-G. Tech. Rep. 18, DKRZ, Hamburg, Germany

Lohmann K, Drange H, Bentsen M (2009) Response of the north atlantic subpolar gyre to persistent north atlantic oscillation like forcing. Climate Dynamics 32:273–285, DOI 10.1007/s00382-008-0467-6

Marshall JC, Schott F (1999) Open ocean convection: Observations, theory and models. Rev Geophys 37-1:1–64

Meehl G, Goddard L, Murphy J, Stouffer RJ, Boer GJ, Danabasoglu G, Dixon KW, Giorgetta MA, Greene AM, Hawkins E, Hegerl G, Karoly D, Keenlyside N, Kimoto M, Kirtman B, Navarra A, Pulwarty R, Smith DM, Stammer D, Stockdale T (2009) Decadal prediction: Can it be skillful? Bull Amer Meteor Soc 90:14671485, DOI 10.1175/2009BAMS2778.1

Meehl GA, Stocker TF, Collins WD, Friedlingstein P, Gaye AT, Gregory JM, Kitoh A, Knutti R, Murphy JM, Noda A, Raper SCB, Watterson IG, Weaver AJ, Zhao ZC (2007) Global Climate Projections, in *Climate Change 2007: The Physical Science Basis. Contribution of Working Group I to the Fourth Assessment Report of the Intergovernmental Panel on Climate Change*, Cambridge University Press, Cambridge, United Kingdom and New York, NY, USA

Monahan A, Alexander J, Weaver A (2008) Stochastic models of the meridional overturning circulation: time scales and patterns of variability. Phil Trans R Soc A 366:2525–2542, DOI 10.1098/rsta.2008.0045

Msadek R, Frankignoul C (2009) Atlantic multidecadal oceanic variability and its influence on the atmosphere in a climate model. Climate Dynamics 33:45–62, DOI 10.1007/s00382-008-0452-0

Pohlmann H, Jungclaus JH, Köhl A, Stammer D, Marotzke J (2009) Initializing Decadal Climate Predictions with the GECCO Oceanic Synthesis: Effects on the North Atlantic. J Clim 22:3926–3938, DOI 10.1175/2009JCLI2535.1

Reynaud TH, Weaver AJ, Greatbatch RJ (1995) Summer mean circulation of the northwestern atlantic ocean. J Geophys Res 100:779–816

Roberts M, Wood R (1997) Topographic sensitivity studies with a bryan–cox-type ocean model. J Phys Oceanography 27:823–836

Roeckner E, Arpe K, Bengtsson L, Christoph M, Claussen M, Dumenil L, Esch M, Giorgetta M, Schlese U, Schulzweida U (1996) The atmospheric general circulation model ECHAM4: model description and simulation of present-day climate. Tech. Rep. 218, Max-Planck-Institut fuer Meterologie, Hamburg, Germany

Saravanan R, McWilliams J (1997) Stochasticity and Spatial Resonance in Interdecadal Climate Fluctuations. J Clim 10:2299–2320

Smith DM, Cusack S, Colman A, Folland C, Harris G, Murphy J (2007) Improved Surface Temperature Prediction for the Coming Decade from a Global Climate Model. Science 317:796–799, DOI 10.1126/science.1139540

von Storch H, Zorita E, Jones JM, Dimitriev Y, Gonzalez-Rouco F, Tett SFB (2004) Reconstructing Past Climate from Noisy Data. Science 306:679–682, DOI 10.1126/science.1096109

Sutton RT, Hodson DLR (2005) Atlantic Ocean Forcing of North American and European Summer Climate. Science 309:115–118, DOI 10.1126/science.1109496

Te Raa L, Dijkstra H (2002) Instability of the thermohaline ocean circulation on interdecadal timescales. Journal of Physical Oceanography 32:138–160

Timmermann A, Latif M, Voss R, Grötzner A (1998) Northern Hemispheric Interdecadal Variability: a Coupled Air-Sea Mode. J Clim 11:1906–1931

Colin de Verdière A, Huck T (1999) Baroclinic instability: An oceanic wavemaker for interdecadal variability. Journal of Physical Oceanography 29(5):893–910

Wolff JO, Maier-Reimer E, Legutke S (1997) The Hamburg Ocean Primitive Equation Model. Tech. Rep. 13, DKRZ, Hamburg, Germany

Zorita E, González-Rouco JF (2002) Are temperature-sensitive proxies adequate for North Atlantic Oscillation reconstructions? Geophys Res Lett 29:48–1, DOI 10.1029/2002GL015404

Zorita E, González-Rouco JF, Legutke S (2003) Testing the Mann et al. (1999) approach to paleoclimate reconstructions in the context of a 1000-yr control simulation with the ECHO-G coupled climate model. J Clim 16:1378–1390
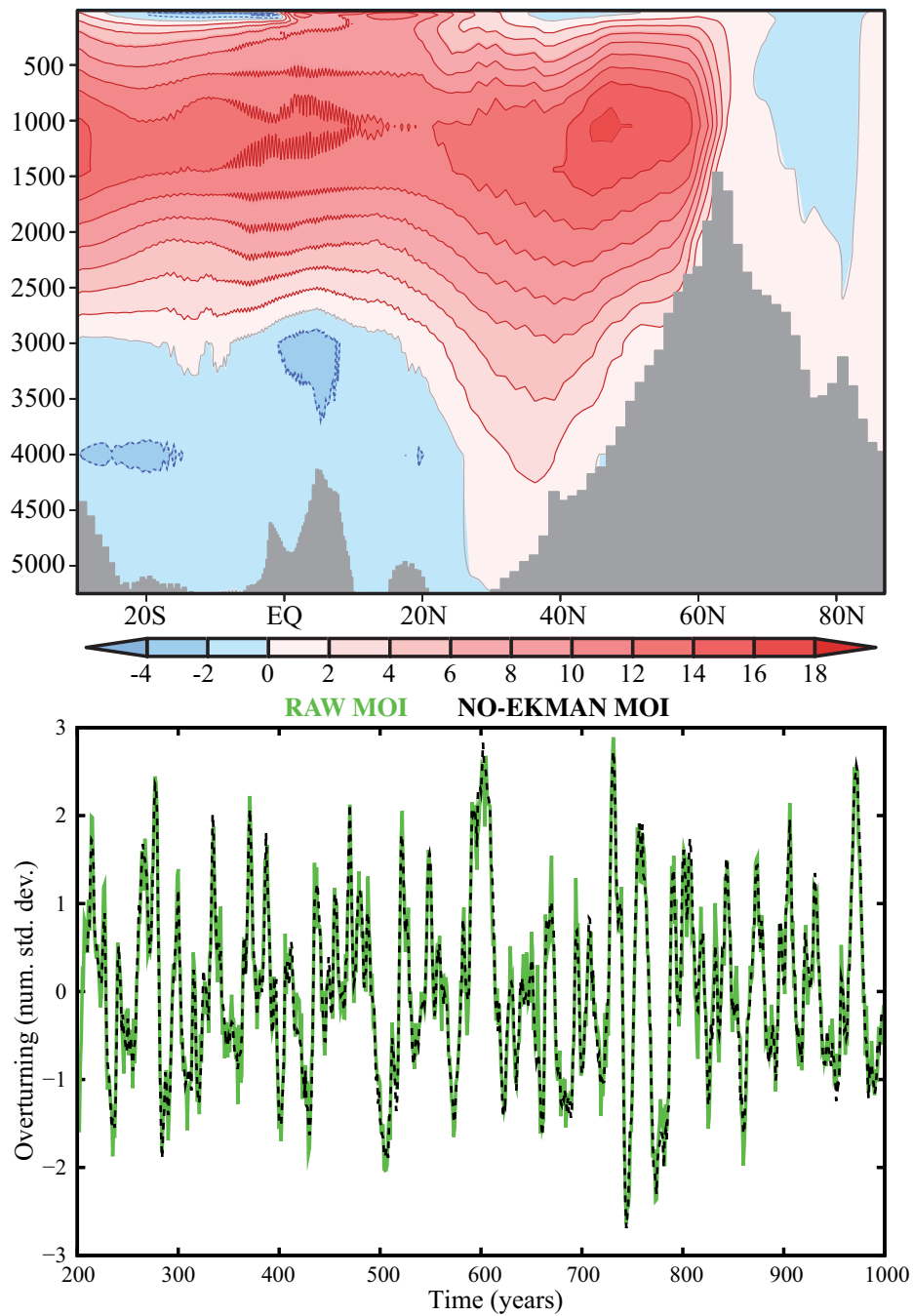
Fig. 1 a) Long-term mean climatology of the meridional streamfunction (in Sv); b) Time series of the normalised Meridional Overturning Index (in std. dev.), defined as the local overturning at 1050m and 47.4° N (climatological maximum). The dashed line represents the MOI after removing the Ekman signal. Note that the standard deviation of the MOI is 1.8 Sv.
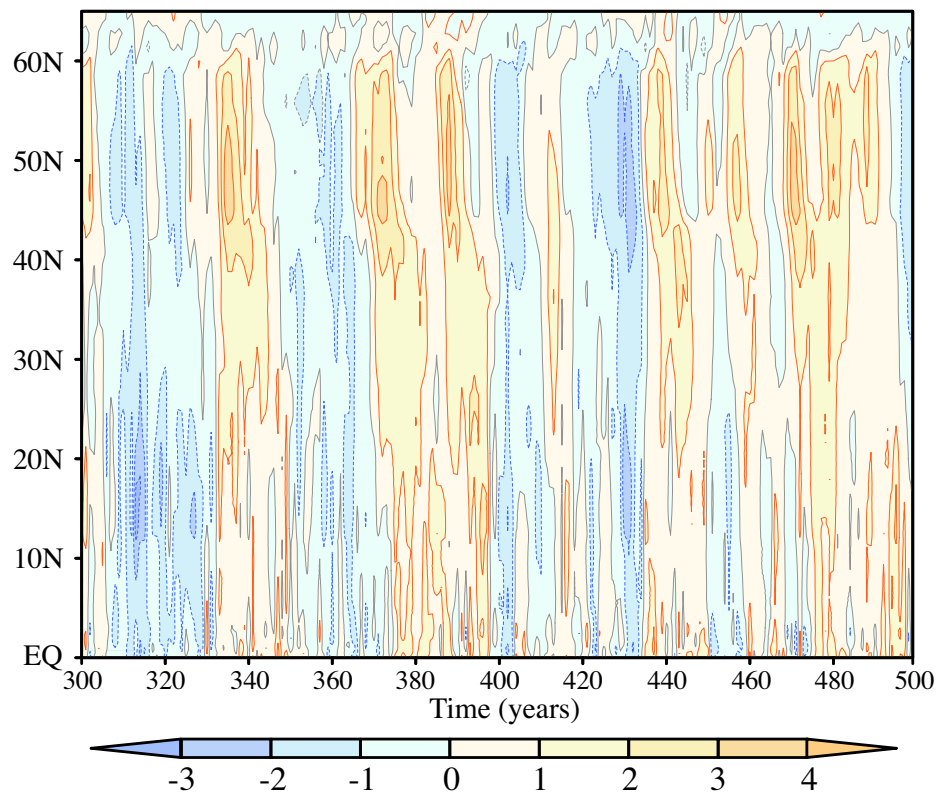
Fig. 2 Zonally averaged northward transport anomalies integrated between 100 and 1050 m depth (in Sv). Note the two different timescales of variability in tropical and extra-tropical latitudes and southward propagation of anomalies.
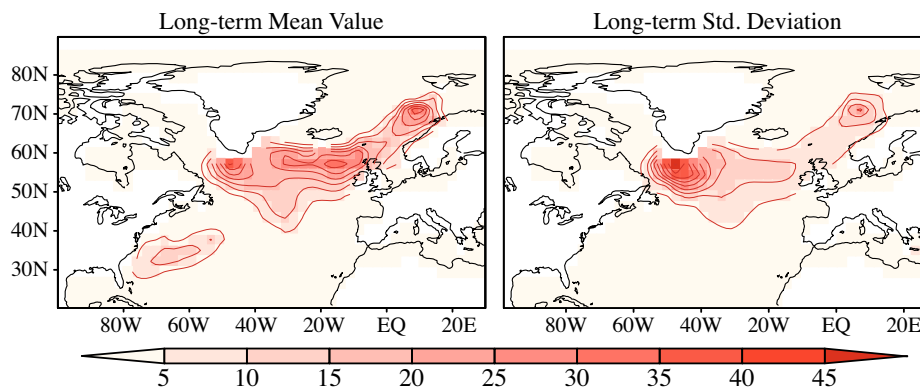
Fig. 3 (a) Long-term mean and (b) standard deviation of the Potential Energy Released by Convection (PERC; in W/m^2) in March.
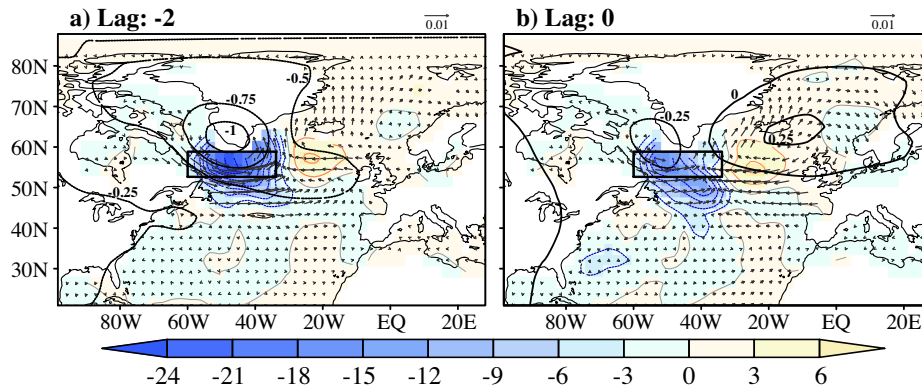
Fig. 4 Regression patterns between the normalised MOI and the anomalies of heat flux (shaded, in W/m^2 per std. dev. of the MOI), the wind-stress (vectors, in N/m^2 per std. dev. of the MOI) and the sea level pressure (black contours, in hPa). Two different lags are considered: (a) the heat flux wind-stress and sea level pressure leading by 2 years and (b) all variables in phase with the MOI. The black rectangle delimits the region where the HFL index is defined.
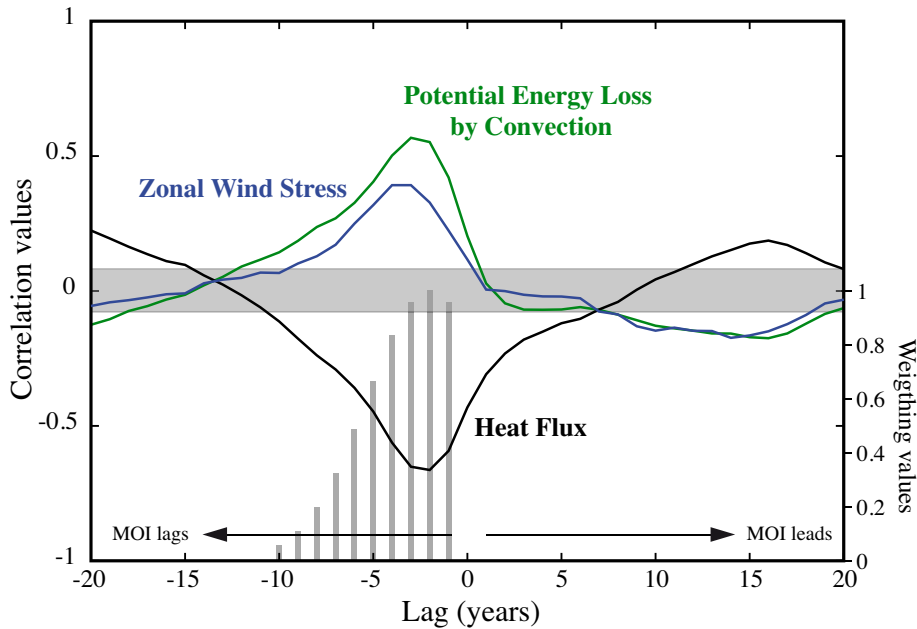
Fig. 5 Time-lag correlations between the MOI and the average of ocean and atmospheric variables in the convection region (box in Figure 4). The shaded region delimits the 5% significant domain. The grey vertical bars show the temporal weighting scheme employed to integrate the first predictor (HFL index).
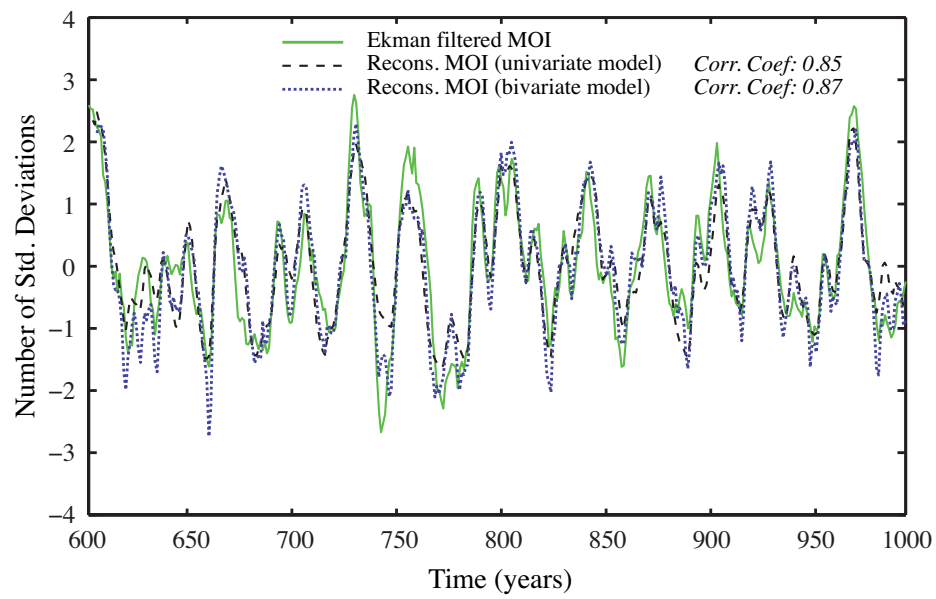
Fig. 6 Time series of the true (Ekman-filtered; green) and reconstructed MOI during the second half of the CTRL simulation (years 600-1000) for the univariate (black) and bivariate (blue) regression models. The correlations between the reconstructed and the true MOI are in italics.
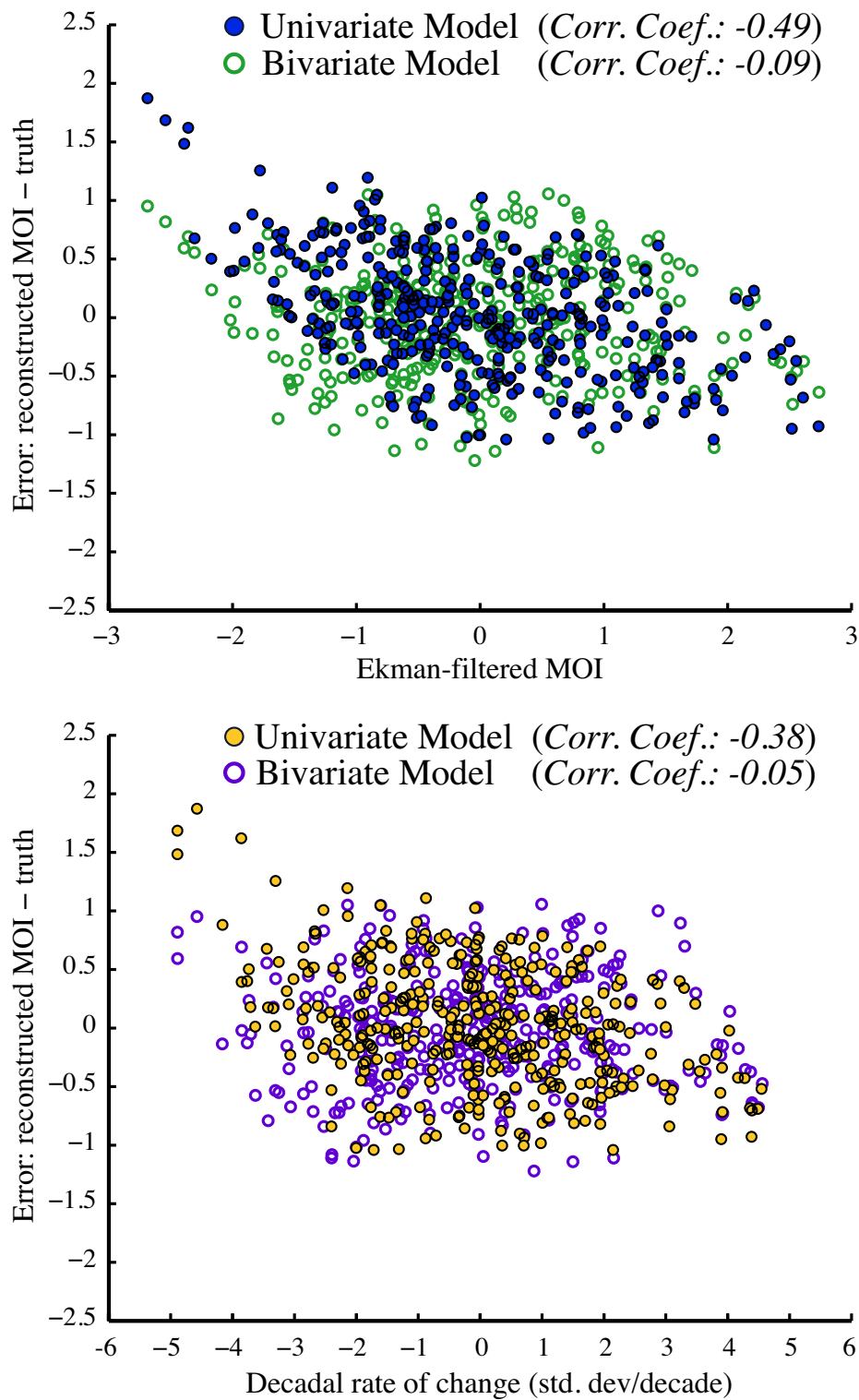
Fig. 7 Scatter plots between the residuals from the regression models and both the Ekman-filtered anomalies of the MOI (top) and the decadal rates of change (bottom). All these results correspond to the second half of the CTRL simulation.
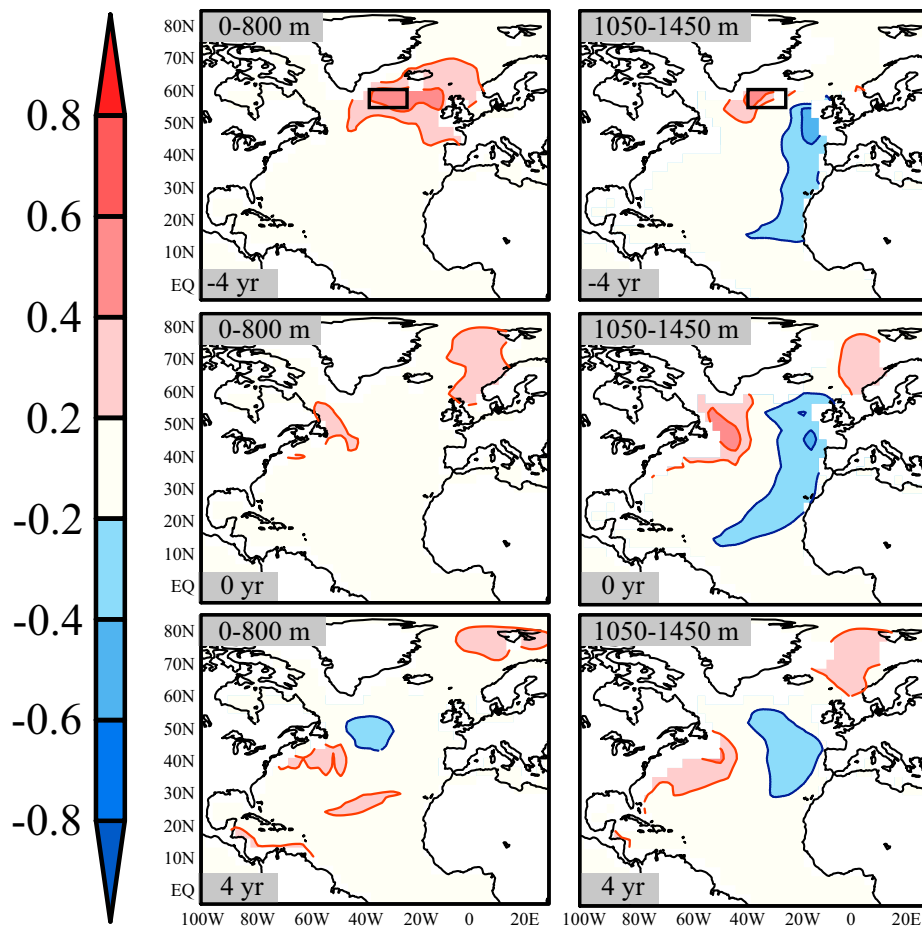
Fig. 8 Lagged cross-correlation patterns between the residuals of the univariate model and the mean values of density for 2 different depth ranges. The black box indicates the region where the second predictor (ISD) is averaged.
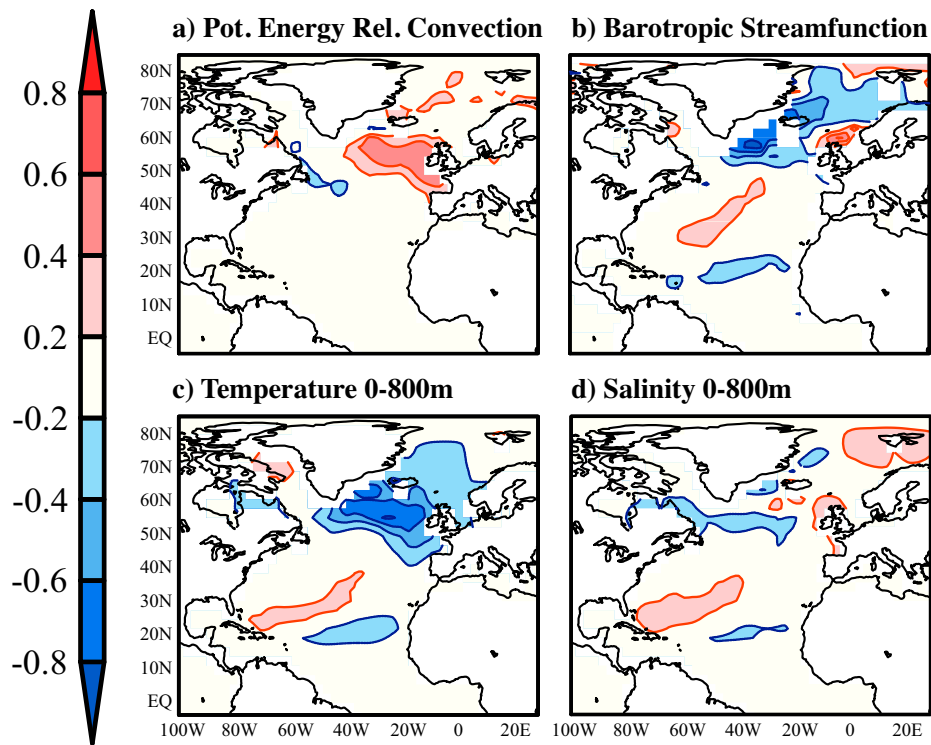
Fig. 9 Lagged cross-correlation patterns between the second predictor and four ocean variables: (a) the potential energy released by convection, (b) the barotropic streamfunction, (c) and (d) the averages of temperature and salinity in the upper 800m.
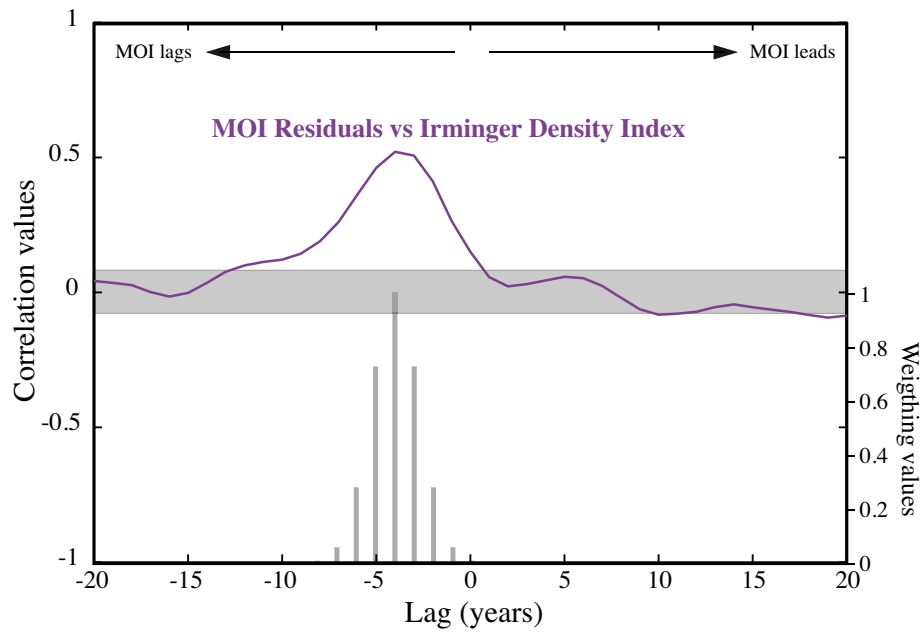
Fig. 10 Time-lag correlations between the residuals of the univariate model and the second predictor (ISD; calculated as the average of density at the upper 1500m of the Irminger Sea; grey box in Figure 8). The shaded region delimits the 5% significant domain. The grey vertical bars show the temporal weighting scheme employed to integrate this predictor.
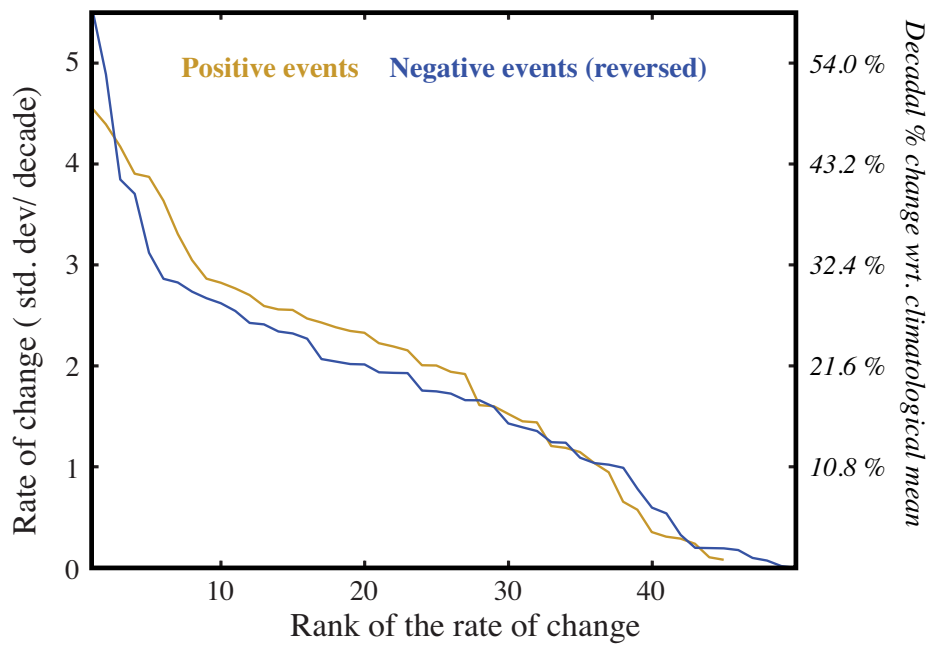
Fig. 11 Decadal rate of change of the large, rapid overturning events ordered in decreasing magnitude (in std. dev./ decade). Note that the sign of the negative events has been reversed to allow comparison with the positive events.
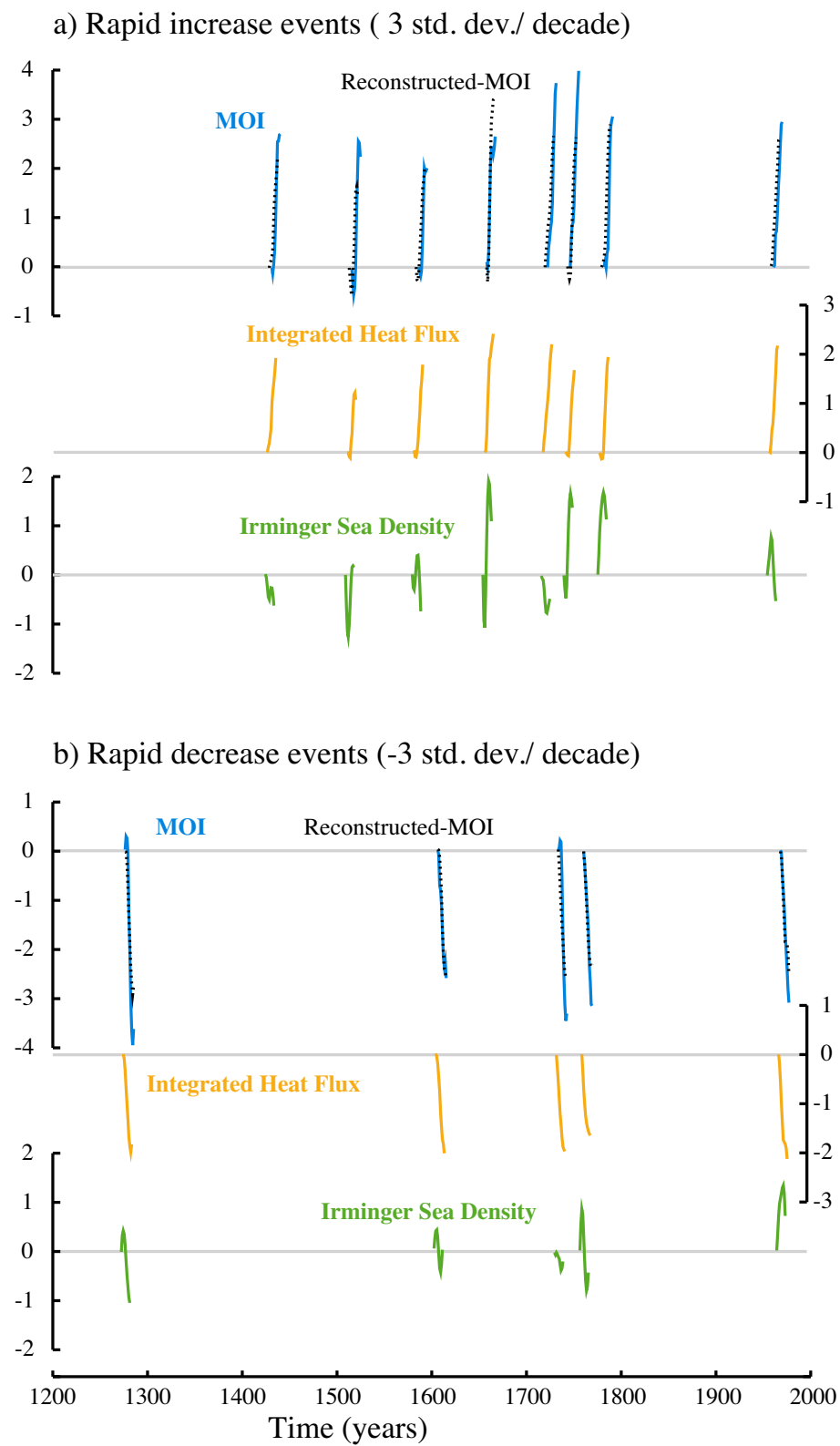
Fig. 12 Evolution of the original Ekman-filtered MOI (blue), the reconstructed index (black) and the predictors (yellow and green) during the largest, rapid decadal overturning events (change above 3 std dev./decade, i.e: 5.4 Sv/decade). Note that the HFL sign is reversed to ease the comparison with the other variables.